Improved modeling of Mars' HDO cycle using a Mars' Global Climate Model

Margaux Vals[1], Loïc Rossi[1], Franck Montmessin[1], Franck Lefèvre[1], Francisco Gonzalez-Galindo[2], Anna Fedorova[3], Mikhail Luginin[3], François Forget[4], Ehouarn Millour[4], Oleg Korablev[3], Alexander Trokhimovskiy[3], Alexey Shakun[3], Antoine Bierjon[4], Luca Montabone[5]

[1]LATMOS/IPSL, UVSQ Université Paris-Saclay, Sorbonne Université, CNRS, Guyancourt, France
[2]Instituto de Astrofísica de Andalucía-CSIC (IAA), Granada, Spain
[3]Space Research Institute (IKI), Moscow, Russia
[4]Laboratoire de Météorologie Dynamique/IPSL, Sorbonne Université, ENS, PSL Research University,Ecole Polytechnique, CNRS, Paris France
[5]Space Science Institute, Boulder, CO, USA

Key Points:

- The HDO cycle has been implemented in the last version of the LMD Mars GCM including microphysics and radiative effect of water ice clouds.
- Kinetics effect is now included in HDO fractionation during condensation and proves to be significant.
- Supersaturation, the presence of which is regulated by cloud processes, alters significantly the relative abundances of HDO and H_2O.

Corresponding author: Margaux Vals, margaux.vals@latmos.ipsl.fr

Abstract

HDO and the D/H ratio are essential to understand Mars past and present climate, in particular with regard to the evolution through ages of the Martian water cycle. We present here new modeling developments of the HDO cycle with the LMD Mars GCM. The present study aims at exploring the behaviour of the D/H ratio cycle and its sensitivity to the modeling of water ice clouds and the formulation of the fractionation by condensation. Our GCM simulations are compared with observations provided by the Atmospheric Chemistry Suite (ACS) on board the ESA/Roscosmos Trace Gas Orbiter, and reveal that the model quite well reproduces the temperature and water vapor fields, which offers a good basis for representing the D/H ratio cycle. The comparison also emphasizes the importance of modelling the effect of supersaturation, resulting from the microphysical processes of water ice clouds, to correctly account for the water vapor and the D/H ratio of the middle-to-upper atmosphere. This work comes jointly with a detailed comparison of the measured D/H profiles by TGO/ACS and the model outputs, conducted in the companion paper of Rossi et al. 2022 (this issue).

Plain Language Summary

The D/H ratio observed in a planetary atmosphere is traditionally used as a proxy to estimate the initial water reservoir of the planet. We present here an improved global circulation model including HDO, the main isotope of water on Mars. The updated model takes into account the details of the formation of clouds and their radiative effect. It also includes the effect of photochemistry on HDO and deuterated species. We find that supersaturation is key to the representation of the D/H cycle by making the hygropause more porous, allowing more HDO in the upper atmosphere. It also reduces the efficiency of the isotopic fractionation occuring at condensation. We present here comparisons between observations by the ACS spectrometer onboard the orbiter TGO. While the model is globally in agreement with the observations, the inability of the model to reproduce the observed vertical distribution of dust, especially during the Global Dust Storm, cause discrepancies in the representation of water vapour. The model reveals the importance of representing the process of supersaturation to correctly account for the water vapor amount reaching the top of the atmosphere and estimate the D/H ratio at escape.

1 Introduction

The D/H ratio is commonly used to constrain the amount of water that was present initially on Mars. Because the light hydrogen atom escapes more easily to space than deuterium, the D/H ratio of the martian atmosphere is 5 to 6 times higher than the Earth's oceans (Owen et al., 1988; Encrenaz, T. et al., 2018; Krasnopolsky, 2015; Villanueva et al., 2015). This is often viewed as a testimony of a progressive loss of water that has made its heavier isotope accruing over time. Furthermore, the D and H atoms populating the exosphere, where they can escape, are initially produced from their precursors H_2O and HDO in the lower atmosphere. H_2O tends to be preferentially photolysed, because of its lower absorption cross-section (Cheng et al., 1999), while HDO is preferentially condensed because of its lower vapor pressure (Bertaux & Montmessin, 2001). These isotopic-dependent processes reduce the ability of deuterium to access the upper atmosphere, and thus its escape rate in comparison to hydrogen.

Deciphering the main mechanisms that control the D/H cycle on Mars is key to understanding how escape has affected the evolution of water on the planet. The recent martian missions provide new insights into this problematic by profiling for the first time D/H ratio (Vandaele et al., 2019; Chaufray et al., 2021; Alday et al., 2021a; Villanueva et al., 2021). In addition, numerical models complete the investigation by helping to interpret the physical processes observed.

In this paper, we refine the modeling of the HDO cycle that was initially developed by Montmessin et al. (2004), and recently re-implemented in the current version of the Martian Global Climate Model (GCM) of the Laboratoire de Météorologie Dynamique (LMD) by Rossi et al. (2021). This work is part of the perspective of a detailed analysis of the D/H ratio behavior based on model outputs and TGO/ACS observations (see companion paper Rossi et al. 2022, this issue).

Condensation-induced fractionation, used in Rossi et al. (2021), makes the HDO cloud cycle mainly dependent on H_2O cloud formation. Cloud formation is a key feature of the H_2O cycle, in particular, microphysics and radiative effect of water ice clouds have been shown to be essential to physically reproduce the observed water cycle with the LMD GCM (Madeleine et al., 2012; Navarro et al., 2014). Microphysics comprise nucleation, ice growth and scavenging of dust. Modeling these different processes allows supersaturation to build up in the model. A phenomenon that is known to exist in the atmosphere of Mars (Maltagliati et al., 2011; Fedorova et al., 2020; Belyaev et al., 2021). Also, radiative effect of water ice clouds have been shown to play a crucial role in the temperature field and, consequently, in the global circulation. In this paper we incorporate a HDO cloud formation model into a GCM including microphysics and radiative effect of clouds, and study the impact on the HDO and D/H cycles. Within the fractionation by condensation, we also implement the effect of kinetics, which moderates the HDO condensation reaction depending on the saturation conditions. To make our model consistent with the detailed analysis of the D/H cycle observed by TGO/ACS (see companion paper Rossi et al. 2022, this issue), we compare the model outputs to TGO/ACS temperature, water vapor and saturation data in the extreme conditions of the MY34 Global Dust Storm.

Section 2 describes the model. Section 3 describes the upgrades implemented for the modeling of the HDO cycle. Section 4 analyzes the results obtained with the new simulations. Section 5 confronts the model outputs of the water cycle in comparison to TGO/ACS observations. Section 6 discusses the results in comparison to TGO/ACS observations and the consequences for the D/H cycle. Section 7 summarizes the conclusions of the paper and proposes perspectives of this work.

2 Description of the model

2.1 General

The model used in this paper is the Martian Global Climate Model (GCM) developed at the Laboratoire de Météorologie Dynamique (LMD) in collaboration with several European teams (LATMOS, IAA Granada, University of Oxford, The Open University) (Forget et al., 1999). A detailed overview of the model, including the last implementations regarding the dust and water cycles, is provided by Navarro et al. (2014). Nevertheless, a brief description of the main modeling features of these two cycles is given in the following paragraphs.

Airborne dust is represented by a two-moment scheme, i.e. by two atmospheric tracers, accounting for both the dust particle number mixing ratio and the dust mass mixing ratio (Madeleine et al., 2011). The effective radius of the dust particles is then derived from these two moments assuming a log-normal distribution. The dust tracers are incorporated into to a "semi-interactive" scheme (Madeleine et al., 2011), which simultaneously allows the free evolution of the vertical distribution of dust, going through the different physical parametrizations, and ensures the match of the integrated column dust opacity to the observed values, as compiled by Montabone et al. (2015); Montabone et al. (2020), for the radiative transfer calculations.

The atmospheric water is represented by two tracers, accounting for the ice and vapor mixing ratios. The implementation of the radiative effect of water ice clouds (Madeleine et al., 2012), shown to have a major impact on the global circulation, has led to the need to finer represent the processes of cloud formation. A microphysics scheme, adapted from Montmessin et al. (2002), has been introduced in the model by Navarro et al. (2014) and includes the main processes of nucleation, ice growth and scavenging, allowing the occurrence of supersaturation. The cloud particles are represented by both the amount of condensed water, i.e. the mass mixing ratio of water ice, and the dust particles on which the water has condensed, i.e. the dust particles converted to Cloud Condensation Nuclei (CCN). As for the dust particles, the CCNs follow a two-moment scheme, with their own size distribution, as described in Navarro et al. (2014).

2.2 Modeling of the HDO cycle

The HDO cycle based on the model developed by Montmessin et al. (2004), has been introduced in the most recent version of the GCM Rossi et al. (2021), yet without activating the radiative effect of clouds and the microphysics scheme. We briefly remind the main features of this implementation.

HDO is represented in the model by two tracers, namely its vapor and ice phases. Both tracers of the isotope go through the same physics of the model as the water tracer, and are freely mixed from the surface to the top of the model. The HDO initial atmospheric and surface mixing ratio are imposed in the model with a ratio of 5×VSMOW. The effect of fractionation by condensation has been introduced in the model presented by Rossi et al. (2021), based on the calculation of a fractionation factor depending on the temperature according to the empirical expression of Lamb et al. (2017):

$$\alpha(T) = \frac{(HDO/H_2O)_{ice}}{(HDO/H_2O)_{vap}} = \exp\left(\frac{13525}{T^2} - 5.59 \times 10^{-2}\right) \quad (1)$$

The condensing mass flux dM_D of HDO can then be expressed from the condensing mass flux dM_H of H_2O as:

$$dM_D = \alpha(T) dM_H \times \frac{M_D}{M_H} \quad (2)$$

where M indicates the mass mixing ratio in the vapor phase, with subscript H referring to water and D to HDO. Finally, as described in Rossi et al. (2021), in the dynamical

part of the model, the isotopic ratio instead of the HDO tracer itself is advected to ensure monotonicity (Risi et al., 2010).

3 Upgrades in modeling the HDO cycle

3.1 HDO combined with microphysics of water ice clouds

In the study of Rossi et al. (2021), the choice was made to use the same simplified cloud model version as in Montmessin et al. (2004). It means the radiative effect of water ice clouds was neglected, as were the details of cloud microphysics (nucleation, ice growth and scavenging), which are necessary to account for supersaturation. In the present paper, we focus on the impact of using the current, detailed, cloud model of Navarro et al. (2014) on the HDO cycle. In practice, it requires to apply the equation (2) on the water condensing mass flux computed at each microphysical timestep.

3.2 Implementation of the effect of kinetics on the fractionation by condensation

Condensation fractionation is complicated by kinetics. Indeed, the higher weight of the isotope HDO restricts its molecular mobility and therefore its ability to diffuse in a gaseous environment compared to H_2O. The molecular diffusion coefficient is a key parameter of the condensation flow. If condensation is not fast enough to maintain an equilibrium between the phases, i.e. to maintain saturation condition, kinetics then significantly affect fractionation. In the experimental framework described by Merlivat and Nief (1967), the vapor to ice conversion is slow enough for the system to remain permanently close to equilibrium, and hence, to isotopic equilibrium. However, ice formation in nature does not necessarily occur in isotopic equilibrium. For example, terrestrial polar ice clouds encounter conditions in which the condensing vapor must diffuse in a strongly supersaturated air (120 % relative humidity, Jouzel and Merlivat (1984)). In situ titrations of deuterium in ice clearly showed that the effect of actual fractionation was not reproduced by Equation (1) (Jouzel & Merlivat, 1984). This formulation had to include the effect of kinetics. Once taken into account, this correction makes it possible to obtain a valid relation under real conditions, where the kinetic fractionation coefficient α_c is expressed in function of the fractionation coefficient of the isotopic equilibrium, obtained with Equation (1), and the ratio of saturation of water vapor S:

$$\alpha_c = \frac{\alpha S}{\alpha(D_{H_2O}/D_{HDO})(S-1)+1} \tag{3}$$

Where D_{H_2O} and D_{HDO} are the coefficients of diffusion of respectively H_2O and HDO. The HDO flux is then calculated as in equation 2 with α_c instead of α.

3.3 Photochemistry of HDO

The photodissociation of HDO has been implemented in the latest version of the photochemical module coupled to the LMD GCM, described in Lefèvre et al. (2021). The HDO absorption cross-sections considered in the model are those measured at 295 K by Cheng et al. (2004) (125-140 nm) and Chung et al. (2001) (140-195 nm). The HDO cross-section is assumed to be identical to that of H_2O shortward of 125 nm.

The process of photolysis is particularly important from around 40 to 60 km altitude. HDO presents a lower absorption cross section to solar UV, which preserves HDO from photolysis relative to H_2O and thus refrains the release of Deuterium atoms. The model also disposes of a vertical extension up to the exobase around 250 km and fully represents the photochemical reactions occurring at these altitude ranges (Angelats i Coll et al., 2005; González-Galindo et al., 2013). This part was completed with the photo-

chemical reactions of the deuterated species, both in the neutral and ionized form, based on Yung et al. (1988).

4 Model results and sensitivity

GCM simulations presented in this section have all been run with a horizontal resolution of 64×48 grid points, corresponding to $\sim 5.625°$ resolution in longitude at the equator and $\sim 3.75°$ resolution in latitude, and 32 vertical levels. The vertical resolution irregularly decreases from ∼2 m close to the surface, to correctly resolve the planetary boundary layer, to ∼5 km close to the top of the model located around 120 km altitude. For the study described in this section, photochemistry and the extension to the thermosphere introduced in Section 3.3, are not included, as they are computationally expensive. Their effect will nevertheless be studied and discussed in Sections 5 and 6. The D/H ratio of both the atmosphere and the surface ice have been initialized to the value of 5× VSMOW. The dust load scenario used in the simulations corresponds to the "climatology" one, typical for a martian year without a global dust storm. The initial state for the presented simulations has been obtained after 10 Martian years of simulation in which the HDO modeling upgrades presented in Section 3, i.e. radiatively active clouds, microphysics and kinetics, were activated. In this section, we focus on the particular season of perihelion, around $L_s = 270°$, for the comparison between the different simulations. This season is the most challenging in modeling as it corresponds to the dust storm season, and is particularly critical for the hydrogen escape as emphasized in Alday et al. (2021b). All Figures of the Section display the fields during daytime (local time 14:00), when the altitude of the hygropause is supposed to be the highest and escape rate the most efficient.

4.1 Effect of radiatively active clouds and microphysics on the D/H cycle

In this section we study the separate impact of radiatively active clouds (RAC) and of microphysics on the D/H cycle. In particular, supersaturation, which is the main consequence of using improved microphysics, is analyzed. Figure 1 shows the zonal mean of temperature, water vapor superimposed with water ice contours, and D/H ratio of the vapor phase superimposed with the seasonal stream functions, at the Southern Hemisphere Summer solstice $L_s = 270°$ and at local time 14:00 for three cases of simulation: one with all processes activated (RAC, microphysics and kinetics), which is referred to as the reference simulation ([REF]), and two other simulations, where RAC and supersaturation have been alternately deactivated (respectively called [RAC OFF] and [supersat OFF] ; see details on how we perform this simulation in Section 4.1.2), all other parameters being equal. Figure 2 shows the difference between the different fields of the different simulations, including a fourth simulation corresponding to the initial case of simple physics of clouds used in Rossi et al. (2021) (simulation called "simple", for "simple physics of clouds").

4.1.1 Impact of RAC

We analyse the difference observed between simulations [REF] and [RAC OFF] to isolate the effect of radiatively active clouds on the D/H cycle. Differences between the two simulations are depicted by Figures 2a, 2b and 2c. During daytime (here at local time 14:00), the main effect of adding the RAC is the warming of the middle atmosphere between 10 and 1 Pa at the low to mid-latitudes, and at the high latitudes (enhanced polar warming). The consequence of such an increase of temperature is the enhancement of the global circulation, illustrated by the streamfunctions shown in Figures 1c and 1f. This effect was already reported in Madeleine et al. (2012) and Navarro et al. (2014). Both effects of increasing temperature and enhancing circulation impact the water cy-

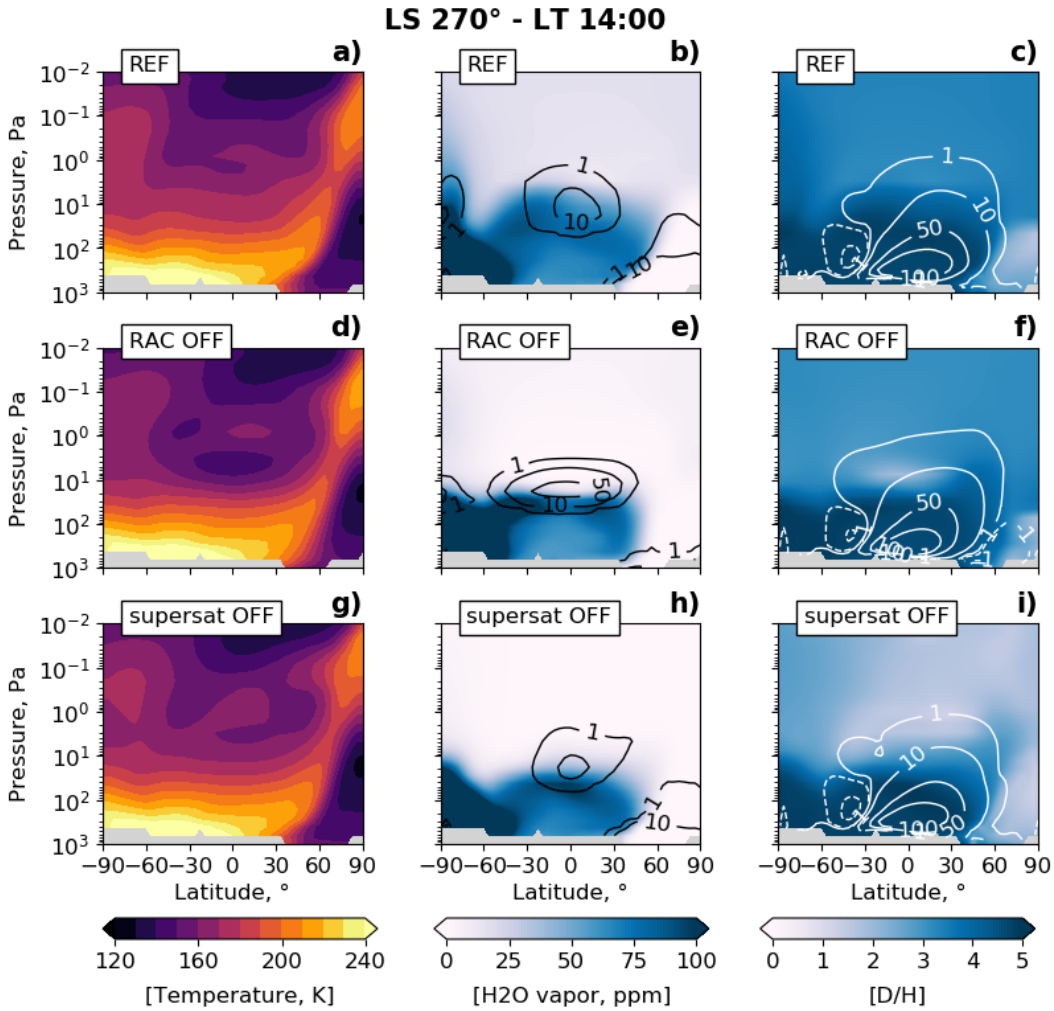

Figure 1. Meteorological variables output of the model zonally averaged at LT=14:00 around $L_s = 270°$ [REF] Results for the reference GCM simulation with radiative effect and microphysics of clouds. [RAC OFF] Results for the GCM simulation in which radiative effect of clouds is turned off. [supersat OFF] Results of the GCM simulation in which the suspersaturation has been turned off. (Left column) Temperature (K). (Middle column) H_2O ice mixing ratio (ppm). (Right column) D/H ratio of the vapor phase. White contours are the stream function in 10^8 kg s^{-1} averaged over Ls= $240° - 270°$.

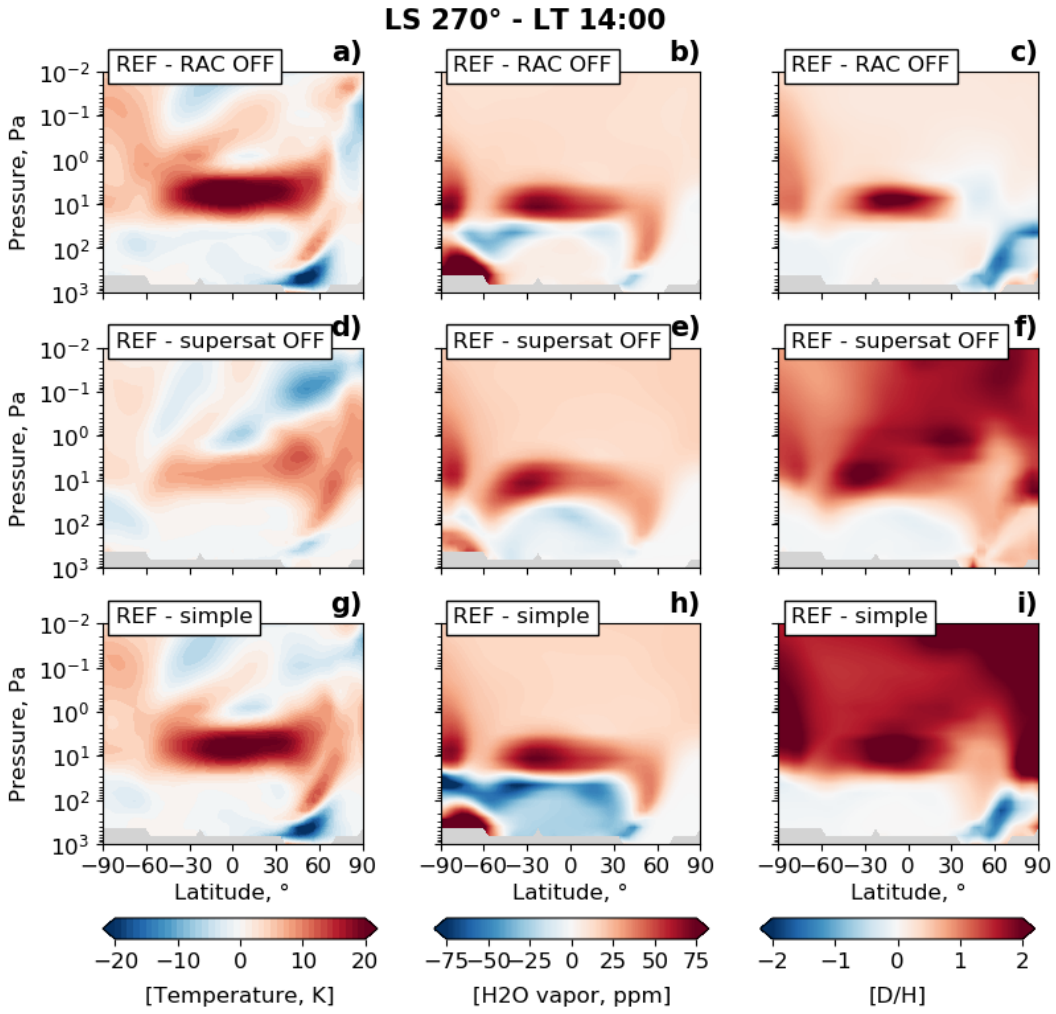

Figure 2. Meteorological variables output of the model zonally averaged at LT=14:00 around $L_s = 270°$ [REF -RAC off] Difference between the meteorological fields of the GCM simulation [REF] and the GCM simulation [RAC OFF]. [REF - supersat OFF] Difference between the meteorological fields of the GCM simulation [REF] and the GCM simulation [supersat OFF]. [REF -simple] Difference between the meteorological fields of the GCM simulation [REF] and the GCM simulation run with simple physics of clouds, i.e. deactivated radiative effect and microphysics [simple]. (Left column) Difference of temperature (K). (Middle column) Difference of the H_2O vapor mixing ratio (ppm). (Right column) Difference of D/H ratio of the vapor phase. Panel c) also displays the contours of saturation in the case of the simulation [REF].

cle, on the one hand by rising the hygropause altitude, and, on the other hand, by fostering the distribution of water higher in the atmosphere. The concentration of water vapor is increased by ∼50 ppm at the hygropause in the low-to-middle latitudes, so as in the South pole near to the surface, and by ∼20 ppm in average in the atmosphere above the hygropause. The concentration of ice clouds is decreased by ∼20% around 10 Pa in the middle atmosphere at low-to-middle latitudes. These ice clouds also show a different structure, spanning a wider altitude range and centered to the tropics, instead of being spread over all latitudes in [RAC OFF]. More water ice (tens of ppm) is also observed in [REF] at the North Pole. The D/H ratio is increased by two in the middle altitudes between 10 and 1 Pa, where the temperature increase and the cloud depletion are observed. The radiative effect of clouds tends to warm the atmosphere between 10 and 1 Pa, which impedes condensation and thus fractionation and explains the corresponding higher D/H ratio of the vapor phase. However, a slightly lower D/H ratio is observed at higher altitude in the area of the polar warming and of the Northern pole. This can be inferred from the presence of thicker ice clouds in [REF] than in [RAC OFF] seen in the North pole, which create a stronger fractionation in these latitudes and a lower amount of HDO in the vapor phase.

4.1.2 Impact of microphysics and the particular role of supersaturation

The implementation of microphysics in the LMD GCM has been shown to significantly improve the representation of the water cycle by correcting unrealistic biases amplified by the radiative effect of clouds (Madeleine et al., 2012; Navarro et al., 2014). In particular, microphysics now allow supersaturation to exist and build up, which is key to simulate clouds realistically (Navarro et al., 2014; Maltagliati et al., 2011; Urata & Toon, 2013). Indeed, microphysics of clouds involve the conversion of dust to condensation nuclei, and the release of this dust in the atmosphere right below the cloud level where water ice particles fall and then sublimate. Nucleation and condensation depend on the availability of dust nuclei and the formation of clouds may be inhibited by a previous episode of scavenging that left condensation level devoid of nuclei. Thus the model is now able to reproduce the emergence and further growth supersaturation, which is observed in the martian atmosphere (Maltagliati et al., 2011; Fedorova et al., 2020). In this part, we focus on the particular role of the presence of supersaturation in the altitude dependence of D/H. In order not to be biased by the radiative effect of clouds, which cannot be correctly represented without activating microphysics, we chose to isolate the effect of supersaturation with a simulation called [supersat OFF]. In this simulation, clouds are still formed with detailed microphysics, including the physical processes of nucleation and ice particle growth, but in the end of each time step, the remnants of supersaturated water vapor are systematically turned into ice. As the number of CCN is however conserved, particles get instantaneously bigger and fall rapidly by sedimentation to the surface. This way, the impact of supersaturation on the altitude dependence of D/H can be addressed.

Results are shown in Figures 2d, 2e and 2f, which correspond to the difference of temperature, water vapor and D/H ratio between the [REF] and [supersat OFF] simulations at Ls=270° and local time 14:00. The temperature field displays an enhanced polar warming effect in the case of [REF] in comparison to [supersat OFF], as shown by 2d). This difference can be inferred from the clouds, which impact on the circulation: the water ice issued from the conversion of supersaturated water vapor in the case of [supersat OFF] involve bigger particles, which fall rapidly to the surface. Therefore, atmospheric water ice is less present in [supersat OFF] than in [REF], i.e. clouds are thinner (see Figures 1b and 1h) and have less radiative impact on the global circulation, which reduces polar warming. Figure 2e reveals that water vapor is redistributed from the lower to the middle-to-upper altitudes in the case of permitted supersaturation, explaining the higher amount (increase by 10 to 50 ppm) predicted in the middle-to-upper atmosphere at all latitudes from around 100 Pa altitude, so as the depletion observed in the lower

altitude ranges. The hygropause is lower in the case of [supersat OFF] and water vapor is confined to lower altitude ranges than in [REF]. The difference in D/H between simulations replicates that of water vapor (see Figure 2e vs. Figure 2f). The global effect of supersaturation at the perihelion season makes the hygropause and the deuteropause more porous, and allows more water vapor to penetrate the middle-to-upper atmosphere while inhibiting fractionation by condensation. Microphysics, especially supersaturation, significantly impact water vapor and ice distributions, which in turn affects the D/H structure essentially by allowing water with a high D/H ratio to migrate towards high altitude.

4.1.3 Impact of RAC and microphysics

Finally we analyse the difference between simulations [REF] and [simple], considering the impact of both effects of microphysics and radiatively active clouds (see Figures 2g, 2h and 2i for the differences between both simulations). The global effect for temperature is almost the same as the difference between simulation [REF] and [RAC OFF]: there is a strong warming at the same locations (see Figure 2g). The water concentration is increased the same way as in the difference between simulation [REF] and [supersat OFF], redistributing water through a more porous and higher hygropause (see Figure 2h). The difference in the D/H ratio illustrates well the combination of both effects with the local increase of D/H around 10 Pa and the increase of D/H in the upper atmosphere (see Figure 2i). This illustrates the impact of both physical processes of microphysics and radiative effect of clouds on the D/H cycle through the impact on the temperature and the water cycle. Both effects significantly impact the distribution of water in the atmosphere, and consequently significantly impact the D/H ratio.

4.2 Effect of the kinetics on the D/H cycle

Taking into account the effect of kinetics in the calculation of the condensation flux of HDO makes the fractionation effect directly dependent on supersaturation. This effect is illustrated by Figure 3, where the HDO vapor mass mixing ratio, and the D/H ratio are displayed respectively for the reference simulation ([REF]) and a simulation in which the effect of kinetics has been turned off ([kinetics OFF]). Kinetics counterbalance fractionation by condensation, as HDO diffuses slower than H_2O in the condensing flux. Equation 2 says that for a given temperature, the higher the saturation, the lower the fractionation coefficient. The correlation between the D/H ratio and the saturation is well illustrated by the contours of saturation showed in Figure 3i.

The global impact of kinetics on the integrated D/H column is shown in Figure 4. The main impact is in the polar nights, where the supersaturation is high. The high fractionation effect occurring at these locations is clearly reduced by kinetics, increasing the D/H from 3 to 4×SMOW.

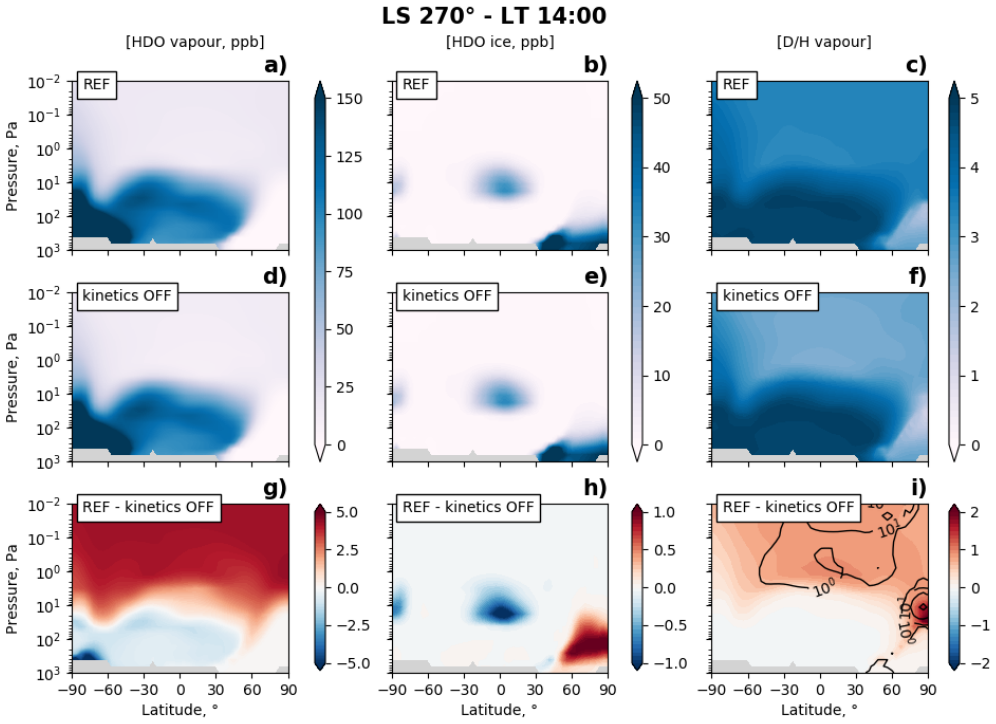

Figure 3. Model outputs of the zonally averaged HDO vapor, HDO ice and D/H at LT=14:00 around $L_s = 270°$ [REF] Results for the reference GCM simulation with radiative effect and microphysics of clouds. [kinetics OFF] Results for the GCM simulation in which the effect of kinetics off fractionation has been turned on. [REF - kinetics OFF] Difference between the two simulations [REF] and [kinetics OFF] described before. (Left column) HDO vapor mixing ratio (ppb). (Middle column) HDO ice mixing ratio (ppb). (Right column) D/H ratio of the vapor phase. The contours of saturation are displayed in the sub-figure i (black contours)

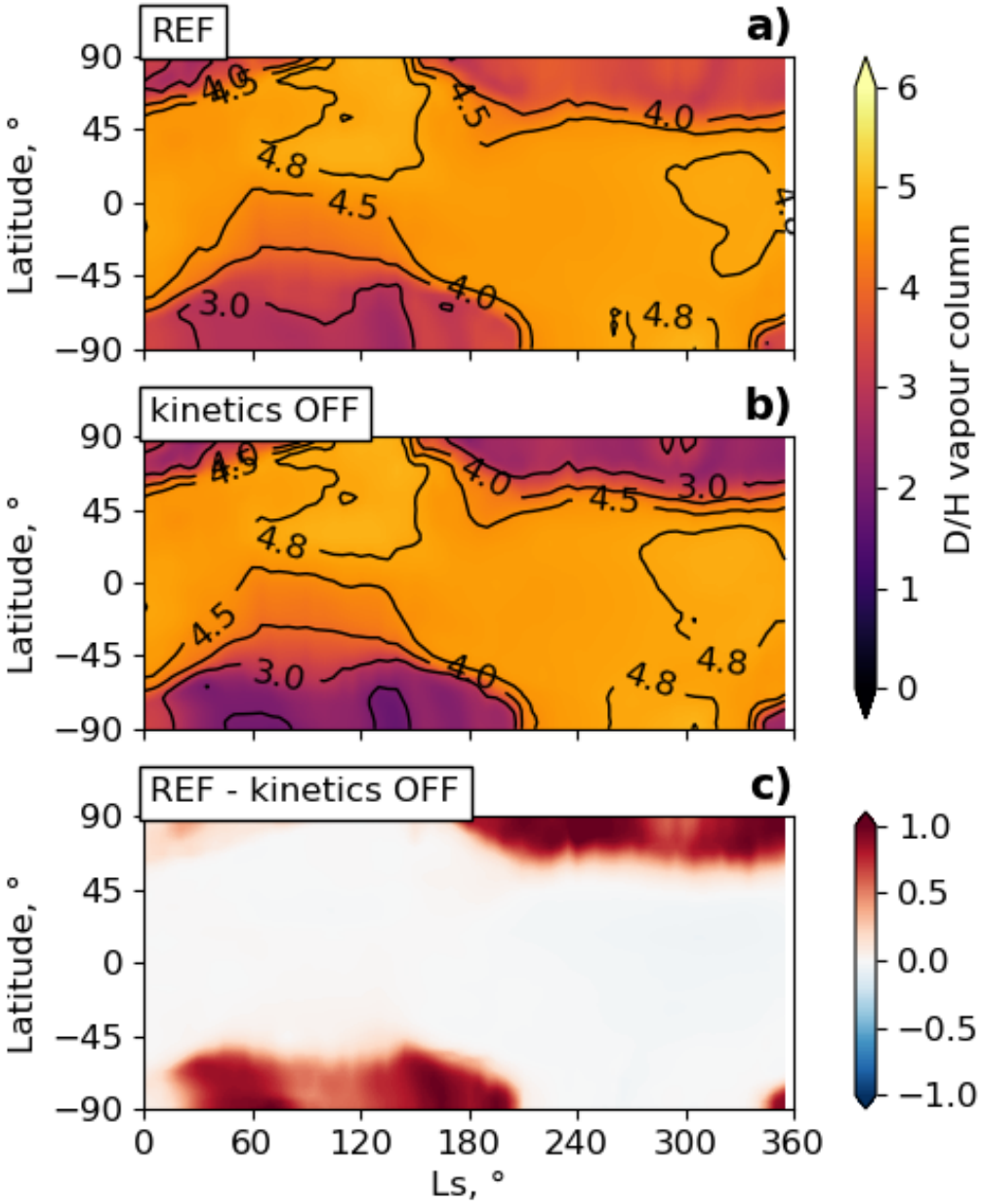

Figure 4. [REF] Zonal average of the D/H integrated water vapor column for the reference GCM simulation with radiative effect, microphysics of clouds and the effect of kinetics on fractionation. [kinetics ON] Zonal average of the D/H integrated water vapor column for the GCM simulation in which the effect of kinetics on fractionation has been turned on. [kinetics ON -REF] Difference between the two simulations [kinetics ON] and [REF] described before.

5 Comparison with observations

In this section, we confront our reference simulation in which all the upgrades of the HDO modeling presented before have been activated, to temperature, H_2O and saturation occultation profiles derived from the TGO/ACS instrument provided by A. Fedorova for the MY34 with the NIR channel (Fedorova et al., 2020). This comparison aims at assessing the validity of the model regarding water and condensation. A detailed comparison between model and observations for HDO is conducted in Rossi et al. 2022 companion paper (this issue).

As mentioned in Navarro et al. (2014) in Section 4.3, the supersaturated water present above the hygropause is exposed to photodissociation, which cannot be neglected in this case. Therefore, the photochemistry module described by Lefèvre et al. (2021), including the upgrades implemented for Deuterium (see Section 3.3), so as the extension to thermosphere, have been turned on in the simulations presented in this section, in order to make the most realistic comparison to the observations. The model outputs, for a simulation run with the MY34 dust scenario of Montabone et al. (2020), have been extracted and interpolated at the same Ls, spatial coordinates (latitude, longitude) and local times as the ACS data. Both, model outputs and data, were interpolated on a vertical grid of 101 levels of 1 km resolution from 0 to 100 km above the areoid.

5.1 Temperature

Figure 5 compares the temperature field produced by TGO/ACS for both hemispheres during MY34 between $L_s = 150°$ and $L_s = 360°$ with the GCM.

The global structure of temperature is overall well reproduced by the model. The model is generally warmer than observations in the upper atmosphere above 50 km in both hemispheres. The temperature field remains warmer even in the model for the case of simple cloud physics without radiative effect of clouds (not shown here), suggesting that it is not linked to cloud formation but to other processes.

The comparison with data from the instrument Mars Climate Sounder onboard Mars Reconnaissance Orbiter (MRO/MCS), provided by L. Montabone, and shown in Figure 6, confirms the warm bias of 20 K, in particular in the higher latitudes and upper altitudes. This bias could be explained by processes not included in the model. For instance, some simulations have shown that taking into account non-orographic gravity waves can reduce the global circulation and, consequently, the polar warming (Gilli et al., 2020). The influence of the CO_2 clouds microphysics, studied with the model in a paper recently submitted by A. Määttänen, is also a factor to be explored, as it could impact the southward returning circulation in the lower atmosphere.

5.2 Water vapor

Figure 7 is the same as Figure 5 but for the H_2O vapor field. As for the temperature, the global structure of the water distribution, including the average altitude of the hygropause, is well reproduced by the model. However, the model presents slightly more water vapor in the upper atmosphere than what is observed, in particular in the northern hemisphere between $L_s = 210°$ and $L_s = 240°$, whereas it fails to reproduce the distinct increase of water vapor between $L_s = 270°$ and $L_s = 300°$ in the southern hemisphere.

The excess of water does not necessarily correlate with the warm temperature bias. Indeed, the difference in water vapor persists in the particular cases where the measured and the modelled temperature finely agree, mainly in the tropical latitudes, like for instance near to $L_s = 240°$ (Figures 8a, 8b and 8c), where saturation is much higher in the model than in the observations. In other cases, as the one displayed in Figures 8c,

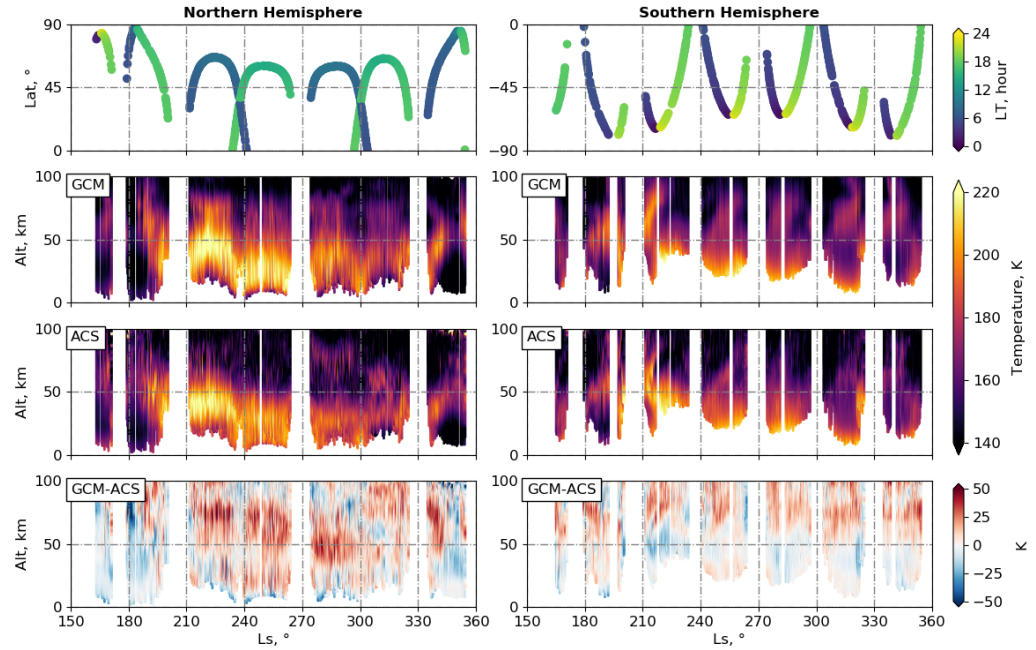

Figure 5. GCM temperature profiles interpolated to the ACS spatial and temporal coordinates, as a function of altitude and solar longitude (Ls). Left column: northern hemisphere, right column: southern hemisphere. First panel corresponds to the data coverage in latitude and local time. Second panel displays the GCM outputs. Third panel shows the ACS data. Fourth panel is the difference between the GCM outputs and the ACS data.

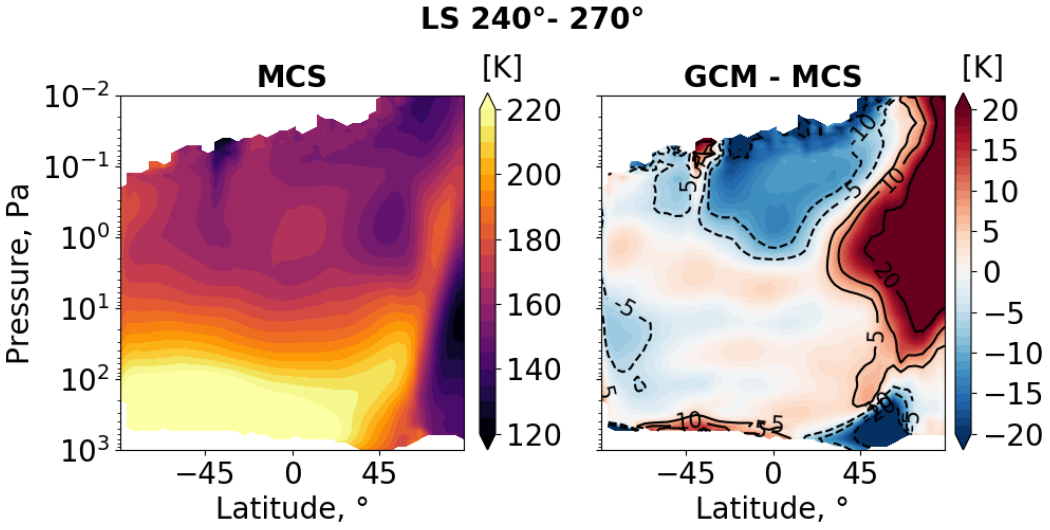

Figure 6. Comparison between the zonal mean daytime temperature at $\sim L_s = 240°$ as measured by MCS and as computed by the GCM. Left panel: MCS temperature field as a function of pressure and latitude, right panel: difference between the GCM outputs and the MCS data.

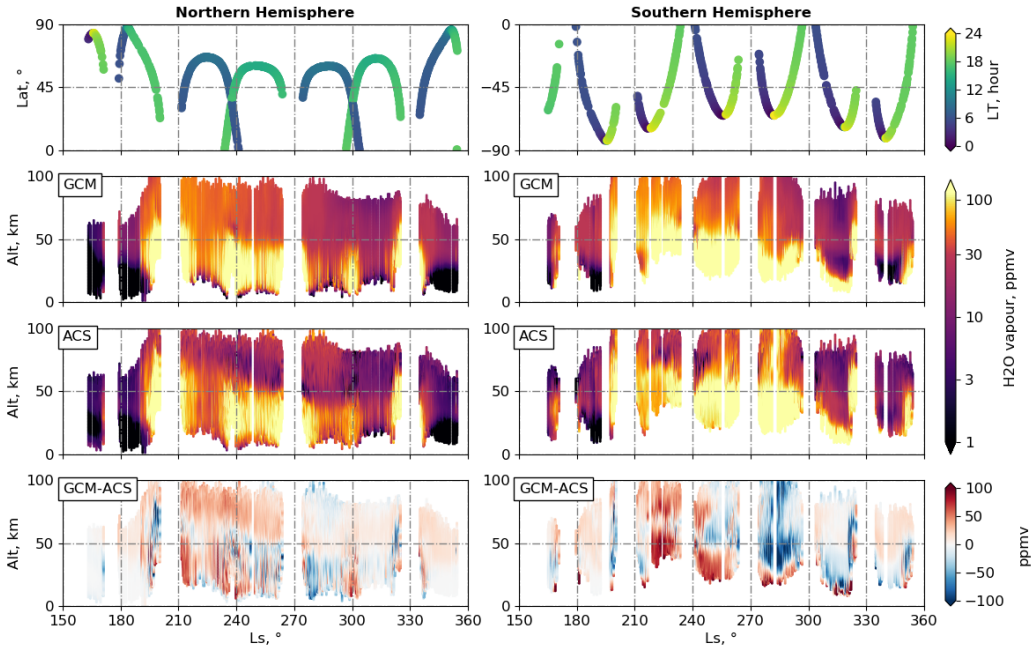

Figure 7. Same layout as Figure 5 but for water vapor volume mixing ratio

8d and 8e, the disagreement in water vapor seems related to the differences in temperature. In this Figure we see that the peak of 300 ppm of water vapor between 40 and 50 km doesn't correspond to supersaturated conditions, but to a slight increase of temperature in the same altitude range.

For both types of profiles presented here, the observed discrepancies between observations and model outputs could be explained by the difficulty of the model to reproduce the dust vertical distribution, in particular during the Global Dust Storm. For orbit 3418 (L_s = 240.0°, Lat=11.3°, LT=6.3 h), shown in 8a, 8b and 8c, the underestimation of condensation, correlated with the excess of supersaturation, could be the result of a lack of dust nuclei in the upper atmosphere. Indeed, ACS observations have identified the presence of water ice clouds at altitudes as high as 80km (Stcherbinine et al., 2020), which are not reproduced by the model. This is also illustrated by Figure 9a that compares GCM outputs with TGO/ACS/TIRVIM and TGO/ACS/NIR ice mass data around the same ranges of solar longitude and latitude as the profile 3418 (Luginin et al., 2020). We can see that the model does not reproduces the water ice amount observed between 60 and 100 km altitude.

For orbit 4192 (L_s = 279.9°, Lat=−62.4°, LT=1.8 h), shown in 8d, 8e and 8f, the layer of warmer temperature observed around 30 to 50 km by ACS, that is also correlated to much higher water vapor mixing ratio, could be the result of detached dust layers created by strong convective activity (Spiga et al., 2013; Daerden et al., 2015; Heavens et al., 2011; Wang et al., 2018; Heavens et al., 2019). In the model, which does not account for these subgrid-scale processes, water vapor is concentrated to lower altitude than observed while the lower hygropause prevents water from reaching higher altitude. This hypothesis is corroborated by Figure 9b which compares GCM outputs with MRO/MCS dust opacity which shows that the dust opacity observed is not well reproduced by the model.

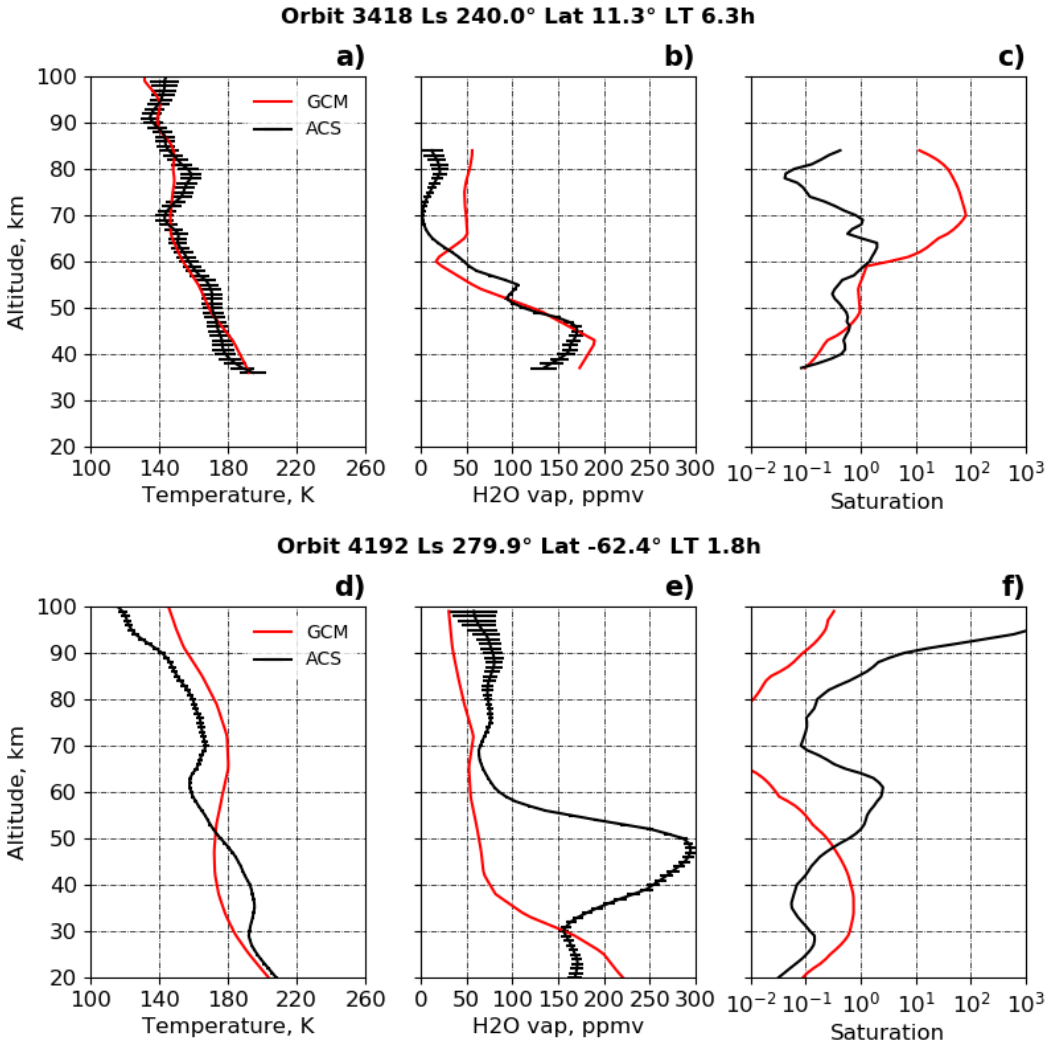

Figure 8. Profiles of temperature, water vapor mixing ratio and saturation in function of altitude corresponding to orbits 3418 (Ls=240.0°, Lat=11.3°, LT=6.3 h) and 4192 (Ls=279.9°, Lat=−62.4°, LT=1.8 h) as measured by ACS (black line) and computed by the GCM (red line).

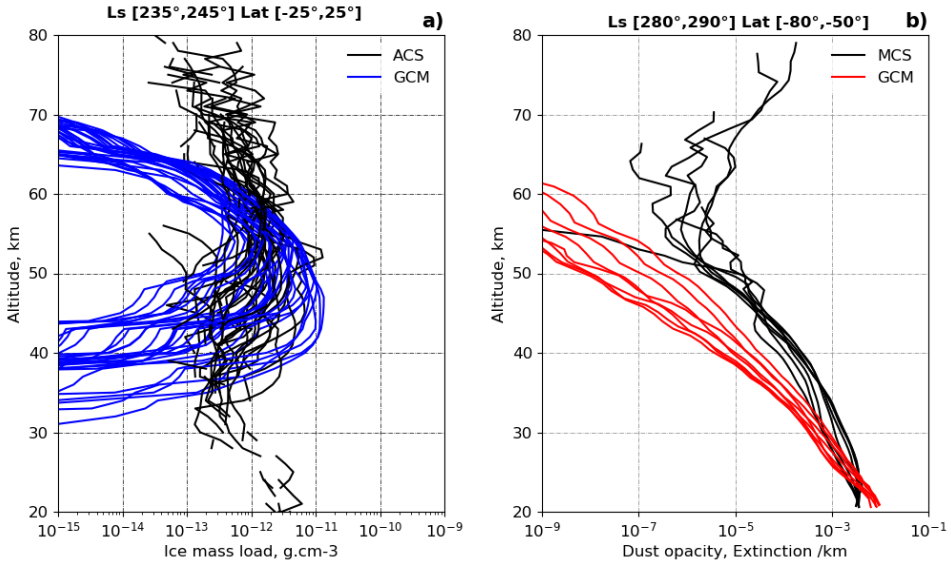

Figure 9. a) Profiles of water ice mass load between $L_s = 235°$ and $L_s = 245°$ and latitude 25°S and 25°N as measured by ACS (black line) and computed by the GCM (blue line). b) Profiles of nighttime dust opacity extinction at wavelength 21.6 μm between Ls=280° and Ls=290° and latitude 60°S and 90°N as measured by MCS (black line) and computed by the GCM (red line).

5.3 Saturation

Figure 10 is the same as Figure 5 but for the saturation field. As for temperature and water vapor, the GCM reproduces the main features of supersaturation observed. However, some disagreements appear and globally correlate with the ones observed in the upper atmosphere (above 50 km) for the water vapor. From $L_s = 210°$ to $L_s = 270°$, saturation in the model is higher than in the observations near 100 km, and from $L_s = 270°$ to $L_s = 300°$ in the Northern Hemisphere. However, observations present higher saturation from 50 to 100 km altitude, which correlates with the colder temperatures. In the Southern Hemisphere, the lack of water vapor seen in the model in comparison with observations between $L_s = 270°$ and $L_s = 300°$ correlates with the lower saturation observed in comparison to TGO/ACS data.

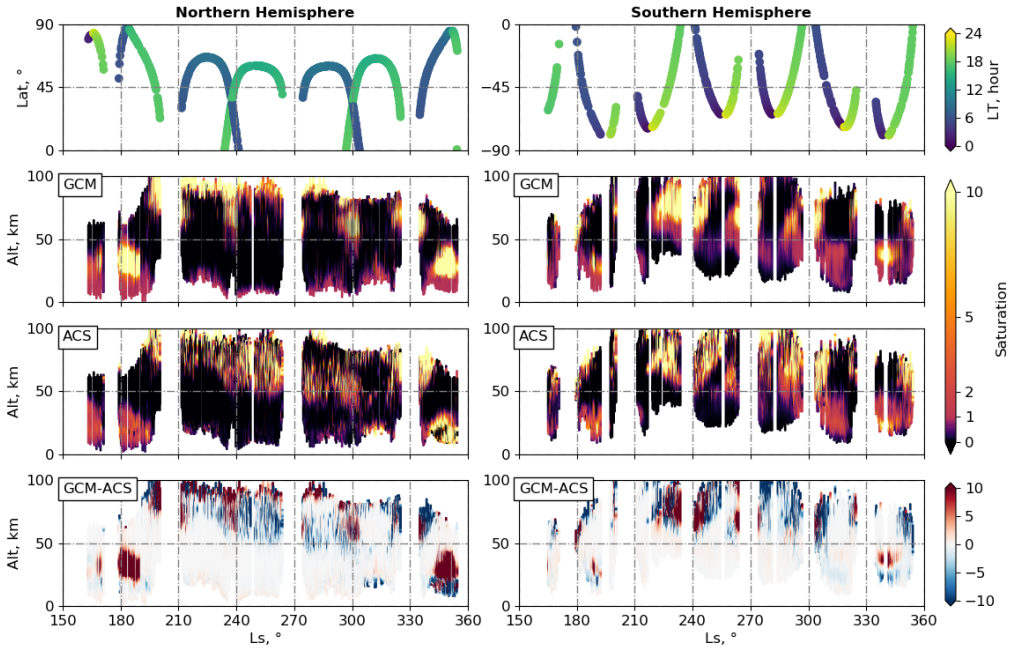

Figure 10. Same layout as Figure 5 but for the saturation

6 Discussion

6.1 Impact of the different physical processes

Figure 11 summarizes the impact of each different physical process implemented in the model and studied in this work. It shows the H_2O and HDO mixing ratios, and the D/H ratio at 80 km altitude, as computed by the model, and interpolated at the ACS measurements coordinates, for a simulation of reference [REF], where all physical packages (RAC, microphysics, kinetics and photochemistry) have been activated, i.e. the simulation used for the comparison with observations in Section 5, and for other experimental simulations, in which each physical process studied has been separately turned off. The impact on D/H of each physical process is detailed hereafter.

As illustrated in Section 4, radiatively active clouds contribute to the presence of water vapor at high altitude. The comparison between [REF] (red dots) and [RAC OFF] (green dots) in Figure 11 reveals that ignoring the radiative effect of clouds significantly degrades the agreement between the model and the observations. Indeed, the amount of water vapor can vary by one ($L_s = 210°$ - $270°$), to two orders of magnitude ($L_s = 270°$ - $330°$) from one simulation to the other. This also has a consequence on the HDO mixing ratio, and on the D/H ratio, which is depleted for the simulation [REF] at 80 km altitude in comparison to simulation [RAC OFF]. This can possibly be explained by the North pole water ice clouds, which are thicker in [REF] than in [RAC OFF] at this season, as illustrated by Figure 2 in Section 4.1.1. The formation of these clouds in [REF] impoverishes the air in deuterium through the global circulation, which results in a lower D/H ratio in the upper atmosphere in comparison to [RAC OFF].

Supersaturation significantly impacts D/H. The comparison between simulations [REF] (red dots) and [supersat OFF] (blue dots) in Figure 11 reveals that ignoring supersaturation results in an underestimation of water vapor of two orders of magnitude

in comparison to the ACS measurements. This proves supersaturation cannot be neglected to realistically reproduce the water amount in the upper atmosphere. This also has a strong impact on D/H, which can be two times lower in the case of not allowing the supersaturation ([SUPERSAT OFF]) than in [REF]. Indeed, according to the model, water vapor in the middle-to-upper atmosphere is in a supersaturated state. Supersaturation makes the hygropause, and the deuteropause more porous, and allows H_2O as well as HDO, penetrate higher altitude ranges than the ones delimited by the water ice cloud level. Both H_2O and HDO amounts increase by two orders of magnitude at 80 km when supersaturation is enabled, as shown by Figure 11. Water can then reach the middle-to-upper atmosphere and becomes exposed to photolysis, subsequently determining the D/H ratio at escape. We also notice that the representation of supersaturation allows the presence of water (tens of ppm) within the middle-to-upper atmosphere as soon as $L_s = 190°$, at the beginning of the storm. There we could have expected that the model, which fails at reproducing the vertical distribution of dust, would not be able to transport water at such high altitudes. This is the case in the model presented by Neary et al. (2020), where supersaturation is not taken into account. Therefore, allowing supersaturation compensates partly for the misrepresentation of the dust dynamics.

The effect of kinetics in the fractionation process is illustrated by Figure 11 with simulations [REF] (red dots) and [kinetics OFF] (purple dots). As this effect only intervenes in HDO fractionation, it does not impact on the comparison of water vapor between the model and the observations (red and purple dots are almost superimposed). As expected, the difference is seen in the mixing ratio of HDO, and consequently in the D/H ratio, which is globally increased by 5% when this process is taken into account.

The comparison between simulations [REF] (red dots) and [photochemistry OFF] (orange dots) in the same figure shows that ignoring photochemistry significantly degrades the agreement between model and observations. This is especially seen within $L_s = 270^\circ - 330°$, where the amount of water vapor is decreased by 25 to 50 % when activating photochemical reactions in both hemispheres. The photolysis is expected to be significant at these altitudes, and is particularly strong near to the perihelion (Clarke et al., 2014; Alday et al., 2021a). The global impact of photochemistry at this altitude is to increase D/H ratio. As H_2O is preferentially photolysed compared to HDO, the D/H ratio of the neutral species is increased. The effect is particularly important around Ls=315° in both hemispheres, where a peak is observed for [REF] and not for [phtochemistry OFF]. These peaks indicate a particularly strong photolysis activity, which can be the result of sampling the descending air from the thermosphere (Hadley circulation near the equinox and the poles), where photolysis is particularly active.

6.2 Global average versus ACS sampling

Considering that ACS sampling is restricted by the TGO orbit which induces a latitudinal drift with time, it is important to question the global representativity of such sampling. This kind of question can be addressed with the model which simulates the entire Martian globe and allows comparing the state of the atmosphere at the sampling locations with the state of the global atmosphere. One expects a bias in this configuration, but does it make ACS and TGO incapable of delivering a consistent appreciation of the entire Martian atmosphere?

Figures 12 and 13 display the global average of the different fields of H_2O and HDO vapor mixing ratio and D/H over both hemispheres compared to the GCM outputs obtained for the reference simulation with the ACS sampling respectively at 80 km and 50 km altitude. Figure 12 shows that at 80 km, although the GCM reproduces the two peaks of water vapor corresponding to the two peaks of dust opacity of MY34 near Ls$\sim$ 190° and Ls$\sim$ 320°, it fails to simulate the increase of water vapor occurring near perihelion in both hemispheres, its intensity being much higher in the southern hemisphere. We

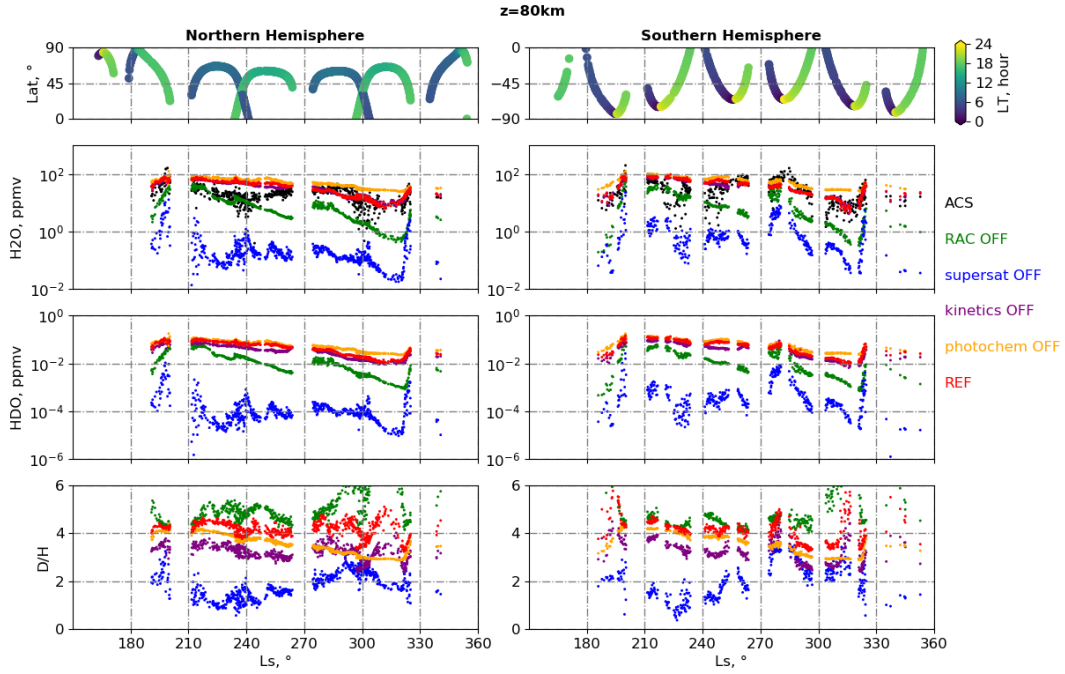

Figure 11. H_2O, HDO and D/H ratio GCM outputs interpolated to the ACS spatial and temporal coordinates at 80 km altitude, as a function of solar longitude (Ls). Left column: northern hemisphere, right column: southern hemisphere. First panel corresponds to the data coverage in latitude and local time. Second row displays the H_2O volume mixing ratio in logarithmic scale. Third row displays the HDO volume mixing ratio in logarithmic scale. Fourth row contains the D/H ratio. GCM outputs are shown for the reference simulation [REF], a simulation in which the supersaturation has been turned off [supersat OFF], a simulation in which the radiative effect of clouds has been turned off [RAC OFF], a simulation in which the effect of kinetics has been turned off [kinetics OFF] and a simulation in which the photochemistry has been turned off [photochem OFF]. ACS water vapor volume mixing ratio are shown in the second row (black dots).

also remark the decrease of water vapor around Ls=240° and Ls=300°, which are not reproduced by the model. As described in Section 4 before, the decrease of water vapor observed between Ls$\sim$ 210° and Ls$\sim$ 270° can be correlated with the presence of water ice clouds not reproduced by the model, because of the lack of dust nuclei transported to these upper altitude ranges. The absence of the peak observed around perihelion in the model can also be attributed to the misrepresentation of the dust vertical distribution, as strong convection transports dust that warms higher altitude and therefore allows water penetration to higher altitude. At 50 km, on the other hand, the model seems to reproduce the observed tendency, except near the perihelion in the southern hemisphere, for the same reasons as at 80 km.

Figure 12 reveals that the ACS sampling is representative of the global behaviour of the atmosphere at 80 km, where the red dots and the blue line follow each other. This is not the case at 50 km, where strong deviations between ACS sampling and global average can be seen. Indeed, the latitudinal coverage of the sampling easily explains the variability of the fields in comparison to the global average over each hemisphere, and we can observe that the water vapor amount at this altitude is increasing with decreasing latitudes. In particular D/H variation appears tightly correlated to the latitudinal sampling. The difference with the global average increases when the sampling approaches the poles, for example in the northern hemisphere between Ls$\sim$ 340° and Ls$\sim$ 350°, where the D/H of the sampling reaches the value of 5$\times$VSMOW, whereas it slowly decreases in the global average around 3.6$\times$VSMOW. The steep increase near both poles disappears, when turning the photochemistry off, which suggests it is due to fractionation by photolysis. As mentioned before, this is the direct effect of sampling near the equinox and the poles, where the air of the descending branch of the Hadley cell comes from the thermosphere, where photodissociation strongly operates.

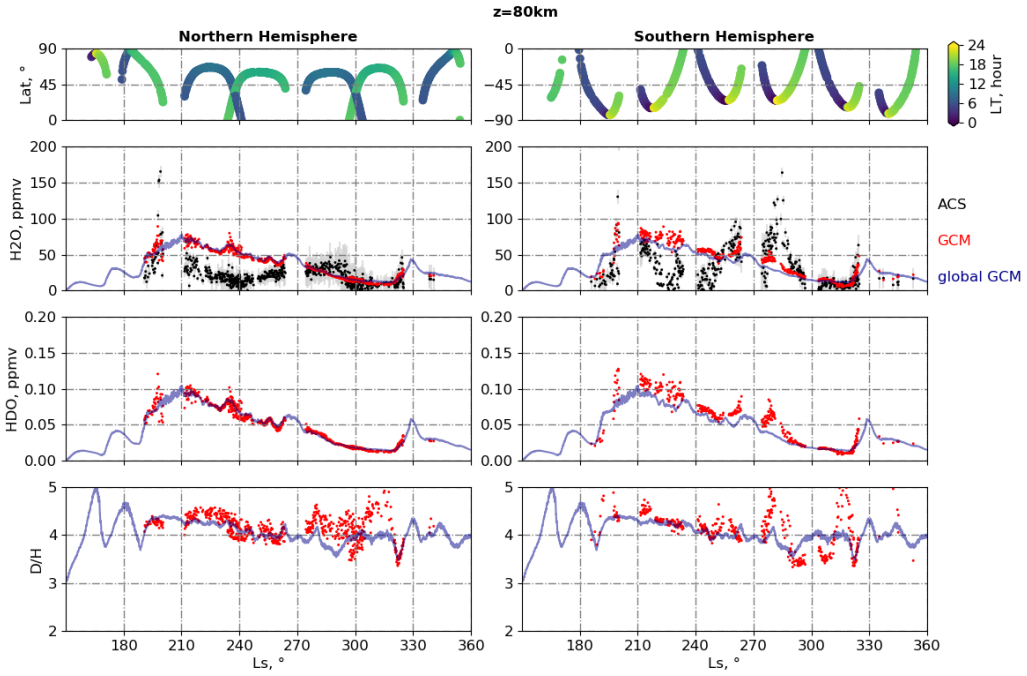

Figure 12. H_2O, HDO and D/H ratio GCM outputs interpolated to the ACS spatial and temporal coordinates at 80 km altitude, and globally averaged over each hemisphere, as a function of altitude and solar longitude (Ls). Left column: northern hemisphere, right column: southern hemisphere. First panel corresponds to the data coverage in latitude and local time. Second row displays the H_2O volume mixing ratio. Third row displays the HDO volume mixing ratio. Fourth row contains the D/H ratio. GCM outputs are shown for the reference simulation [REF] with GCM outputs interpolated to ACS coordinates (red dots), and for the global (zonal and latitudinal) average over each hemisphere (dark blue line). ACS water vapor volume mixing ratio are shown in the second row (black dots).

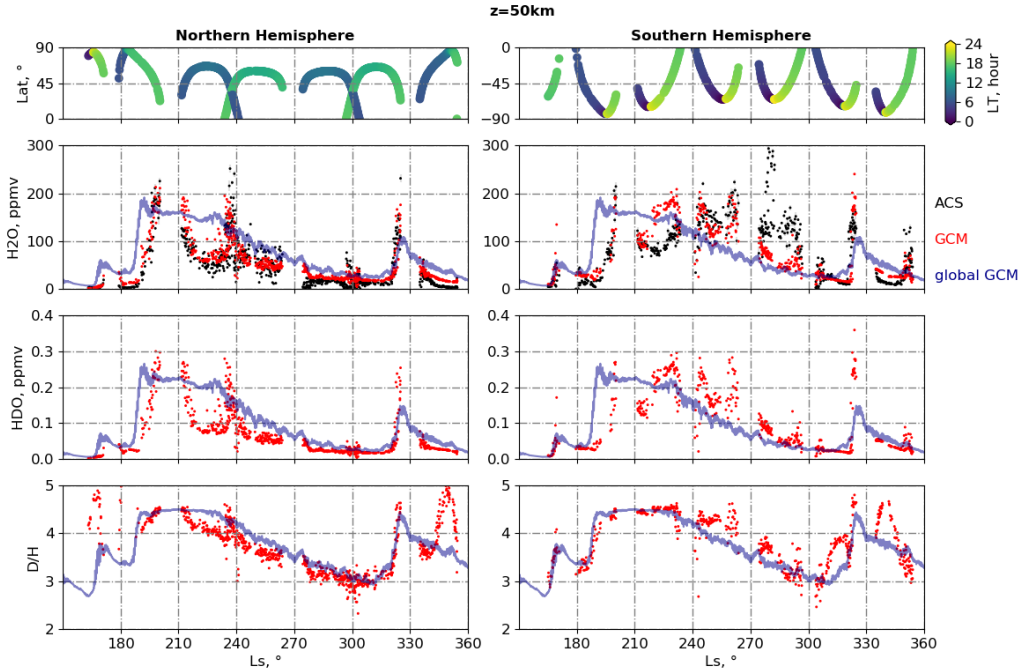

Figure 13. Same layout as Figure 12 at 50 km altitude

7 Conclusion

In this work we have shown the importance of modeling the detailed aspects of the water cycle to correctly account for the D/H cycle and, consequently, for the amount of water potentially escaping from the upper atmosphere. In particular, simulations with the LMD Mars GCM have shown that the radiative effect of clouds and their microphysics tend both to rise the altitude of the hygropause and the deutoropause, and significantly increase the D/H ratio in the middle atmosphere. In particular, the interaction between dust and water ice, responsible for the presence of supersaturation, tends to increase the porosity of the hygropause and deuteropause, allowing water (between 30 to 100 ppm) to penetrate higher altitude ranges (up to 100 km). The implementation of the effect of kinetics in the process of fractionation by condensation has also shown a significant difference in the D/H ratio, correlated with strong saturation. To conclude, supersaturation has two main impacts on the D/H, first by allowing a significant amount of water and HDO vapor to penetrate the upper atmosphere, and second by moderating the process of fractionation by condensation through the effect of kinetics.

The comparison between the TGO/ACS measurements of MY34 and the corresponding GCM outputs reveals a slight overestimation of the water vapor amount of the model in the middle-to-upper atmosphere, where water is in supersaturated state. This overestimation of supersaturation is suspected to result from a lack of dust nuclei present in the upper atmosphere, consequence of the misdealing of the vertical distribution of dust by the model. Supersaturation is also very sensitive to the poorly known "contact parameter" of the condensation nuclei, which is fixed in the model (see Navarro et al. (2014)). Besides, the model fails to represent the large increase of water vapor observed near to the perihelion in the Southern Hemisphere. This could also be attributed to the difficulty to represent the dust vertical distribution, supposed to be particularly controlled by vertical convection mechanisms during the dusty season. Further comparisons between GCM simulations and TGO/ACS observations have also confirmed the importance in

representing supersaturation to correctly account for the water vapor amount present in the middle-to-upper atmosphere.

Finally, this study reveals that the TGO/ACS sampling is quite representative for the global behavior of the atmosphere at high altitude levels (∼80 km), except near the poles, but the agreement is degraded in the middle altitude levels (∼50 km), especially near the poles.

Comparisons of the measured D/H profiles by TGO/ACS and the GCM are studied in the companion paper of Rossi et al. 2022 (this issue). In the near future, the fate of deuterium on Mars will be studied with our GCM by means of a comprehensive description of the deuterium photochemistry and escape. These recent improvements bring us closer fully representing the global D/H cycle, from the surface up to the top of the atmosphere.

Acknowledgments

ExoMars is the space mission of ESA and Roscosmos. The ACS experiment is led by IKI Space Research Institute in Moscow. The project acknowledges funding by Roscosmos and CNES. Science operations of ACS are funded by Roscosmos and ESA.

The data used to produce the figures presented in this article can be obtained on the following link : `https://doi.org/10.14768/9ba77f68-29a3-4bd6-8966-0900e2316a54` The MRO/MCS dust opacity data were provided by Luca Montabone and are available at the same link. The TGO/ACS/NIR temperature and water retrievals used in this study were initially published in Fedorova et al. (2020) and are available at `http://exomars.cosmos.ru/ACS_Results_stormy_water_vREzUd4pxG/`. The TGO/ACS/TIRVIM and TGO/ACS/NIR water ice retrievals were initially published in Luginin et al. (2020) and can be obtained at `https://data.mendeley.com/datasets/rkszdmpdcy/1`. The LMD General Circulation Model is available on request from the LMD team.

We thank the TGO/ACS team, so as Luca Montabone, for treating and providing the data with valuable inputs. We also thank the LMD team, in particular Antoine Bierjon, for providing the tools to correctly handle with the model outputs.

M.V. acknowledges support from the DIM ACAV labelled by the Ile-de-France region in support for the research (Domaine d'Intérêt Majeur, Astrophysique et Conditions d'Apparition de la Vie)". L.R. acknowledges support from CNES.

References

Alday, J., Trokhimovskiy, A., Irwin, P. G. J., Wilson, C. F., Montmessin, F., Lefévre, F., ... Shakun, A. (2021a). Isotopic fractionation of water and its photolytic products in the atmosphere of Mars. *Nature Astronomy*. doi: 10.1038/s41550-021-01389-x

Alday, J., Trokhimovskiy, A., Irwin, P. G. J., Wilson, C. F., Montmessin, F., Lefévre, F., ... Shakun, A. (2021b). Isotopic fractionation of water and its photolytic products in the atmosphere of Mars. *Nature Astronomy*, *5*. doi: 10.1038/s41550-021-01389-x

Angelats i Coll, M., Forget, F., López-Valverde, M. A., & González-Galindo, F. (2005). The first Mars thermospheric general circulation model: The Martian atmosphere from the ground to 240 km. *Geophys. Res. Lett.*, *32*, 4201. doi: 10.1029/2004GL021368

Belyaev, D. A., Fedorova, A. A., Trokhimovskiy, A., Alday, J., Montmessin, F., Korablev, O. I., ... Shakun, A. V. (2021). Revealing a High Water Abundance in the Upper Mesosphere of Mars With ACS Onboard TGO. *Geophysical Research Letters*, *48*(10). doi: 10.1029/2021GL093411

Bertaux, J.-L., & Montmessin, F. (2001). Isotopic fractionation through water vapor condensation: The deuteropause, a cold trap for deuterium in the atmosphere of mars. *Journal of Geophysical Research: Planets*, *106*(E12), 32879-32884. doi: 10.1029/2000JE001358

Chaufray, J. Y., Mayyasi, M., Chaffin, M., Deighan, J., Bhattacharyya, D., Clarke, J., ... Jakosky, B. (2021). Estimate of the D/H Ratio in the Martian Upper Atmosphere from the Low Spectral Resolution Mode of MAVEN/IUVS. *Journal of Geophysical Research (Planets)*, *126*(4), e06814. doi: 10.1029/2020JE006814

Cheng, B.-M., Chew, E. P., Liu, C.-P., Bahou, M., Lee, Y.-P., Yung, Y. L., & Gerstell, M. F. (1999). Photo-induced fractionation of water isotopomers in the martian atmosphere. *Geophysical Research Letters*, *26*(24), 3657-3660. doi: 10.1029/1999GL008367

Cheng, B.-M., Chung, C.-Y., Bahou, M., Lee, Y.-P., Lee, L. C., van Harrevelt, R., & van Hemert, M. C. (2004). Quantitative spectroscopic and theoretical study of the optical absorption spectra of H_2O, HOD, and D_2O in the 125-145 nm region. *Journal of Chemical Physics*, *120*(1), 224-229. doi: 10.1063/1.1630304

Chung, C.-Y., Chew, E. P., Cheng, B.-M., Bahou, M., & Lee, Y.-P. (2001). Temperature dependence of absorption cross-section of H $_2$O, HOD, and D $_2$O in the spectral region 140-193 nm. *Nuclear Instruments and Methods in Physics Research A*, *467*(2002), 1572-1576. doi: 10.1016/S0168-9002(01)00762-8

Clarke, J. T., Bertaux, J. L., Chaufray, J. Y., Gladstone, G. R., Quemerais, E., Wilson, J. K., & Bhattacharyya, D. (2014, November). A rapid decrease of the hydrogen corona of Mars. *grl*, *41*(22), 8013-8020. doi: 10.1002/2014GL061803

Daerden, F., Whiteway, J. A., Neary, L., Komguem, L., Lemmon, M. T., Heavens, N. G., ... Smith, M. D. (2015). A solar escalator on Mars: Self-lifting of dust layers by radiative heating. *grl*, *42*(18), 7319-7326. doi: 10.1002/2015GL064892

Encrenaz, T., DeWitt, C., Richter, M. J., Greathouse, T. K., Fouchet, T., Montmessin, F., ... Sagawa, H. (2018). New measurements of d/h on mars using exes aboard sofia. *A&A*, *612*, A112. doi: 10.1051/0004-6361/201732367

Fedorova, A. A., Montmessin, F., Korablev, O., Luginin, M., Trokhimovskiy, A., Belyaev, D. A., ... Wilson, C. F. (2020). Stormy water on Mars: The distribution and saturation of atmospheric water during the dusty season. *Science*, *367*(6475), 297-300. doi: 10.1126/science.aay9522

Forget, F., Hourdin, F., Fournier, R., Hourdin, C., Talagrand, O., Collins, M., ... Huot., J.-P. (1999). Improved general circulation models of the Martian atmosphere from the surface to above 80 km. *J. Geophys. Res.*, *104*, 24,155-24,176.

Gilli, G., Forget, F., Spiga, A., Navarro, T., Millour, E., Montabone, L., ... Schofield, J. T. (2020). Impact of Gravity Waves on the Middle Atmosphere of Mars: A Non-Orographic Gravity Wave Parameterization Based on Global Climate Modeling and MCS Observations. *Journal of Geophysical Research (Planets)*, *125*(3), e05873. doi: 10.1029/2018JE005873

González-Galindo, F., Chaufray, J. Y., López-Valverde, M. A., Gilli, G., Forget, F., Leblanc, F., ... Yagi, M. (2013). Three-dimensional Martian ionosphere model: I. The photochemical ionosphere below 180 km. *Journal of Geophysical Research (Planets)*, *118*(10), 2105-2123. doi: 10.1002/jgre.20150

Heavens, N. G., Kass, D. M., & Shirley, J. H. (2019). Dusty Deep Convection in the Mars Year 34 Planet-Encircling Dust Event. *Journal of Geophysical Research (Planets)*, *124*(11), 2863-2892. doi: 10.1029/2019JE006110

Heavens, N. G., Richardson, M. I., Kleinböhl, A., Kass, D. M., McCleese, D. J., Abdou, W., ... Wolkenberg, P. M. (2011). Vertical distribution of dust in the Martian atmosphere during northern spring and summer: High-altitude tropical dust maximum at northern summer solstice. *Journal of Geophysical Research (Planets)*, *116*(E15), E01007. doi: 10.1029/2010JE003692

Jouzel, J., & Merlivat, L. (1984). Deuterium and oxygen 18 in precipitation: Modeling of the isotopic effects during snow formation. *jgr*, *89*(D7), 11,749-11,757. doi: 10.1029/JD089iD07p11749

Krasnopolsky, V. A. (2015). Variations of the hdo/h2o ratio in the martian atmosphere and loss of water from mars. *Icarus*, *257*, 377 - 386. doi: https://doi.org/10.1016/j.icarus.2015.05.021

Lamb, K. D., Clouser, B. W., Bolot, M., Sarkozy, L., Ebert, V., Saathoff, H., ... Moyer, E. J. (2017). Laboratory measurements of hdo/h2o isotopic fractionation during ice deposition in simulated cirrus clouds. *Proceedings of the National Academy of Sciences*, *114*(22), 5612–5617. doi: 10.1073/pnas.1618374114

Lefèvre, F., Trokhimovskiy, A., Fedorova, A., Baggio, L., Lacombe, G., Määttänen, A., ... Montmessin, F. (2021). Relationship Between the Ozone and Water Vapor Columns on Mars as Observed by SPICAM and Calculated by a Global Climate Model. *Journal of Geophysical Research (Planets)*, *126*(4). doi: 10.1029/2021JE006838

Luginin, M., Fedorova, A., Ignatiev, N., Trokhimovskiy, A., Shakun, A., Grigoriev, A., ... Korablev, O. (2020). Properties of Water Ice and Dust Particles in the Atmosphere of Mars During the 2018 Global Dust Storm as Inferred From the Atmospheric Chemistry Suite. *Journal of Geophysical Research (Planets)*, *125*(11), e06419. doi: 10.1029/2020JE006419

Madeleine, J.-B., Forget, F., Millour, E., Montabone, L., & Wolff, M. J. (2011, November). Revisiting the radiative impact of dust on Mars using the LMD Global Climate Model. *Journal of Geophysical Research (Planets)*, *116*, 11010. doi: 10.1029/2011JE003855

Madeleine, J.-B., Forget, F., Millour, E., Navarro, T., & Spiga, A. (2012). The influence of radiatively active water ice clouds on the Martian climate. *Geophys. Res. Lett.*, *39*, 23202. doi: 10.1029/2012GL053564

Maltagliati, L., Montmessin, F., Fedorova, A., Korablev, O., Forget, F., & Bertaux, J.-L. (2011, September). Evidence of Water Vapor in Excess of Saturation in the Atmosphere of Mars. *Science*, *333*, 1868-. doi: 10.1126/science.1207957

Merlivat, L., & Nief, G. (1967). Fractionnement isotopique lors des changements d'état solide-vapeur et liquide-vapeur de l'eau à des températures inférieures à 0°c. *Tellus*, *19*(1), 122-127. doi: 10.1111/j.2153-3490.1967.tb01465.x

Montabone, L., Forget, F., Millour, E., Wilson, R. J., Lewis, S. R., Cantor, B., ... Wolff, M. J. (2015). Eight-year climatology of dust optical depth on Mars. *Icarus*, *251*, 65-95. doi: 10.1016/j.icarus.2014.12.034

Montabone, L., Spiga, A., Kass, D. M., Kleinböhl, A., Forget, F., & Millour, E. (2020). Martian year 34 column dust climatology from mars climate sounder observations: Reconstructed maps and model simulations. *Journal of Geophysical Research: Planets*, *n/a*(n/a), e2019JE006111. doi: 10.1029/2019JE006111

Montmessin, F., Fouchet, T., & Forget, F. (2004). Modeling the annual cycle of HDO in the Martian atmosphere . *Journal of Geophysical Research*, *Submitted*.

Montmessin, F., Rannou, P., & Cabane, M. (2002). New insights into Martian dust distribution and water-ice cloud microphysics. *Jour. Geophys. Res. (Planets)*, 4-1.

Navarro, T., Madeleine, J.-B., Forget, F., Spiga, A., Millour, E., Montmessin, F., & Määttänen, A. (2014). Global Climate Modeling of the Martian water cycle with improved microphysics and radiatively active water ice clouds. *Journal of Geophysical Research (Planets)*. doi: 10.1002/2013JE004550

Neary, L., Daerden, F., Aoki, S., Whiteway, J., Clancy, R. T., Smith, M., ... Vandaele, A. C. (2020). Explanation for the Increase in High-Altitude Water on Mars Observed by NOMAD During the 2018 Global Dust Storm. *Geophysical*

Research Letters, *47*(7), e84354. doi: 10.1029/2019GL084354

Owen, T., Maillard, J. P., de Bergh, C., & Lutz, B. L. (1988). Deuterium on Mars: The Abundance of HDO and the Value of D/H. *Science*, *240*(4860), 1767-1770. doi: 10.1126/science.240.4860.1767

Risi, C., Bony, S., Vimeux, F., & Jouzel, J. (2010). Water-stable isotopes in the LMDZ4 general circulation model: Model evaluation for present-day and past climates and applications to climatic interpretations of tropical isotopic records. *Journal of Geophysical Research (Atmospheres)*, *115*, D12118. doi: 10.1029/2009JD013255

Rossi, L., Vals, M., Montmessin, F., Forget, F., Millour, E., Fedorova, A., ... Korablev, O. (2021). The Effect of the Martian 2018 Global Dust Storm on HDO as Predicted by a Mars Global Climate Model. *grl*, *48*(7), e90962. doi: 10.1029/2020GL090962

Spiga, A., Faure, J., Madeleine, J.-B., Määttänen, A., & Forget, F. (2013, April). Rocket dust storms and detached dust layers in the Martian atmosphere. *Journal of Geophysical Research (Planets)*, *118*, 746-767. doi: 10.1002/jgre.20046

Stcherbinine, A., Vincendon, M., Montmessin, F., Wolff, M. J., Korablev, O., Fedorova, A., ... Shakun, A. (2020, March). Martian Water Ice Clouds During the 2018 Global Dust Storm as Observed by the ACS-MIR Channel Onboard the Trace Gas Orbiter. *Journal of Geophysical Research (Planets)*, *125*(3), e06300. doi: 10.1029/2019JE006300

Urata, R. A., & Toon, O. B. (2013). Simulations of the martian hydrologic cycle with a general circulation model: Implications for the ancient martian climate. *Icarus*, *226*, 229-250. doi: 10.1016/j.icarus.2013.05.014

Vandaele, A. C., Korablev, O., Daerden, F., Aoki, S., Thomas, I. R., Altieri, F., ... Zorzano, M. P. (2019). Martian dust storm impact on atmospheric H_2O and D/H observed by ExoMars Trace Gas Orbiter. *Nature*, *568*(7753), 521-525. doi: 10.1038/s41586-019-1097-3

Villanueva, G., Liuzzi, G., Crismani, M. M. J., Aoki, S., Vandaele, A. C., Daerden, F., ... NOMAD team (2021). Water heavily fractionated as it ascends on Mars as revealed by ExoMars/NOMAD. *Science Advances*. doi: 10.1126/sciadv.abc8843

Villanueva, G. L., Mumma, M. J., Novak, R. E., Käufl, H. U., Hartogh, P., Encrenaz, T., ... Smith, M. D. (2015). Strong water isotopic anomalies in the martian atmosphere: Probing current and ancient reservoirs. *Science*, *348*(6231), 218–221. doi: 10.1126/science.aaa3630

Wang, C., Forget, F., Bertrand, T., Spiga, A., Millour, E., & Navarro, T. (2018). Parameterization of Rocket Dust Storms on Mars in the LMD Martian GCM: Modeling Details and Validation. *Journal of Geophysical Research (Planets)*, *123*(4), 982-1000. doi: 10.1002/2017JE005255

Yung, Y. L., Wen, J.-S., Pinto, J. P., Allen, M., Pierce, K. K., & Paulson, S. (1988). HDO in the Martian atmosphere: Implications for the abundance of crustal water. *Icarus*, *76*(1), 146-159. doi: 10.1016/0019-1035(88)90147-9